

# Observational Study of a Gust Front Triggered by Vertical Momentum Transport within a Typhoon

Ahoro Adachi <sup>1</sup>, Takahisa Kobayashi <sup>2</sup>

MRI, 1-1 Nagamine, Tsukuba, Ibaraki 305-0052, Japan, <sup>1</sup>aadachi@mri-jma.go.jp, <sup>2</sup>kobay@mri-jma.go.jp

## ABSTRACT

Observations from a Doppler radar, a wind profiler, and a meteorological tower were used to study the evolution of a thin-line echo that was observed in the radar reflectivity field over the Kanto Plain of Japan as Typhoon Higos (0221) passed in October 2002. The thin-line echo was accompanied by gusty winds and followed by cold airflows, and passed the MRI field site in Tsukuba, Japan. Data from the MRI instrument array and from a surface observation network revealed that the thin-line echo was caused by a gust front.

Although it was demonstrated that the thin-line echo was due to a gust front, this gust front could not be categorized as a so-called thunderstorm gust front because it had no parent thunderstorm; rather, observations showed that the gust front in the present study was generated in a weak precipitation region between the typhoon center and a trailing outer rainband to the southwest. Doppler radar and wind profiler observations suggest that relatively strong downdrafts in the weak precipitation region and large momentum transported by the downdrafts from aloft (~ 4 km) to lower levels produced and maintained near-surface high winds behind the gust front.

## 1. INTRODUCTION

Hurricanes (or typhoons) are among the most destructive and lethal of all natural disasters, and are accompanied by violent winds and heavy rainfall. Most damage and loss of life results from hurricane-force winds and wind-induced storm surges. Hurricane winds are enhanced locally when tornadoes and/or gust fronts develop within a hurricane and cause great damage to surface structures, because the high winds associated with tornadoes and/or gust fronts enhance gusts in hurricanes on or near the ground. Although studies on tornadoes in hurricanes are common, studies on hurricane gust fronts are limited. Such studies are rare because in many cases hurricane gust fronts may be too shallow to detect [1].

Thunderstorm gust fronts have been studied observationally with *in situ* measurements or remote sensors and also through numerical modeling and laboratory simulations. Studies have shown that strong cold downdrafts within or beneath thunderstorms are deflected laterally upon reaching the ground and produce cold-air outflow, whose periphery is a gust front that propagates horizontally away from the storm. The main sources of the strong downdrafts are hydrometeor evaporation, i.e., convective downdrafts, and precipitation drag.

Recent studies have shown that momentum transfer by downdrafts also contributes damaging winds associated with gust fronts (e.g., [2]). However, the contribution of momentum transport by the downdrafts to the generation of hurricane gust fronts has not been reported despite the large momentum aloft in hurricanes.

Typhoon Higos passed across the Kanto Plain of Japan in October 2002. The MRI Doppler radar observed a thin-line echo propagating in the radar reflectivity field associated with the typhoon. The line echo passed the MRI field site in Tsukuba, Japan, and peak surface wind gusts at the site were  $31.6 \text{ m s}^{-1}$ . In addition, a peak wind gust of  $58.8 \text{ m s}^{-1}$  was observed at 70 m AGL on the top of a transmission line tower at the passage of the thin-line echo about 30 km west of the MRI site. This means that gusts with wind speeds comparable to those of F2 tornadoes accompanied the thin-line echo.

Similar thin-line echoes are often observed with gust fronts. However, gust fronts are not the only causes of thin-line echoes, so this is not proof that such echoes are due to gust fronts. In this paper, thus, we describe the evolution and reveal the cause of the thin-line echo that occurred as Typhoon Higos passed using data from the MRI instrument array and from surface observations. We especially focus on the contribution of momentum transport by the downdrafts to the generation of the surface wind gusts associated with the thin-line echo.

## 2. DATA AND METHODOLOGY

The MRI operates a 5.7-cm-wavelength Doppler radar that is mounted on top of the MRI building. Reflectivity and mean radial Doppler velocity in the operational data products were used in this study. Doppler radar observations at the MRI field site are complemented by a network of surface instruments, Automated Meteorological Data Acquisition System (AMeDAS) and observations from a 213-m meteorological tower and a wind profiler. Table 1 lists operating parameters for the MRI Doppler radar system and the wind profiler.

Table 1. Parameters of the MRI Doppler Radar and WP

	Doppler	Profiler
Frequency	5260 MHz	1357.5 MHz
Peak power	250 kW	2 kW
Beam width	$1.01^\circ$	$4^\circ$
Unambiguous range	160 km	7.5 km
Range gate spacing	250 m	100 m
Max unfolding velocity	$53.6 \text{ m s}^{-1}$	$17.3 \text{ m s}^{-1}$
Temporal resolution	~ 6 min	~ 15 s

### 3. OVERVIEW OF THE THIN-LINE ECHO

#### 3.1 Satellite and Radiosonde Observations

Figure 1 shows Geostationary Meteorological Satellite infrared imagery at 21 JST (Japan Standard Time: JST = UTC + 9 hours) on 1 October 2002. Typhoon Higos is making landfall in the observation area over eastern Japan. A downward arrow points to the region of cold IR temperatures ( $T_b < 215$  K). This region corresponds to mature convection over the Kanto Plain. The altitude of the cloud top as inferred from  $T_b$  exceeded 14 km. Prior hourly satellite images (not shown) indicate that this high cloud corresponded to the eyewall of Higos. The right-pointing arrow points to a dark narrow region that is to the west of the high cloud. This dark region includes a region where cloud top heights as inferred from  $T_b$  were less than 7 km. This region could be a dry slot, because a dry layer aloft (< 90 % at 1-2.5 km) was observed with a radiosonde that passed through the region launched from the MRI site at 2209 JST. The relatively dry layer might enhance hydrometeor evaporation.

#### 3.2. Surface Measurements and Reflectivity Fields

Figure 2a shows reflectivity at 2136 JST and surface wind vectors and temperature at 2140 JST. The two regions ( $A_2$  and  $A_3$ ) of large reflectivity ( $Z > 35$  dBZ) are evident. The strongest reflectivity in region  $A_2$  was within and moved with the region of high cloud tops defined in Fig. 1. Thus, region  $A_2$  likely corresponds to the region of high cloud tops. In contrast, region  $A_3$  was formed by a merger of two regions ( $A_1$  and B) at 2013 JST as shown later (Fig. 3). Note that south of regions  $A_2$  and  $A_3$  was a mostly rain-free region. This region matches the dark region in Fig. 1.

Figure 2b shows surface wind vectors and sea-level temperature at 2140 JST. A local cold region is evident behind region  $A_3$  at the time. Prior AMEDAS observations (not shown) indicate that this local cold region was formed by 2110 JST just behind region  $A_3$ .

After the cold air mass formed, rain region  $A_3$  moved eastward and narrowed as it extended southeast. As the cold air mass moved eastward, the rain region became concentrated ahead of the cold air mass, where a large temperature gradient occurred (Figs. 2a and 2b). The rain region formed a thin-line echo clearly by 2119 JST; the thin-line echo was then always located at the leading edge of the moving cold air mass (Figs. 2a and 2b). This association is often observed with thunderstorm gust fronts. The thin-line echo passed the MRI at about 2150 JST, with an estimated mean propagation speed and direction of  $19.5 \text{ m s}^{-1}$  and  $71^\circ$ , respectively, clockwise from the north. Winds gusted to  $31.6 \text{ m s}^{-1}$  at the MRI just after the thin-line echo passed.

Note that the thin-line echo was located near the edge of the dark region (Fig. 2a) that corresponded to the region of low cloud tops in the satellite imagery. This means that the thin-line echo was not due to a so-called thunderstorm gust front because it had no parent thunderstorm. We next explore the mechanism that formed the thin-line echo associated with the gusty winds.

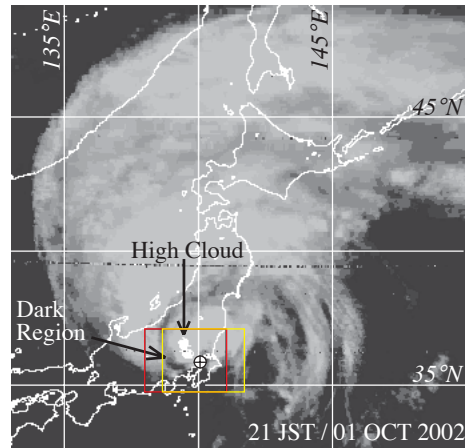


Figure 1. GMS-5  $T_b$  imagery of Typhoon Higos at 21 JST. The cross symbol within an open circle denotes the typhoon center. The downward arrow indicates a high cloud ( $T_b < 215$  K), and the right-pointing arrow points to a dark region that includes low clouds ( $T_b > 263$  K). The rectangles indicate the analysis areas for Figs. 2a (yellow) and 2b (red).

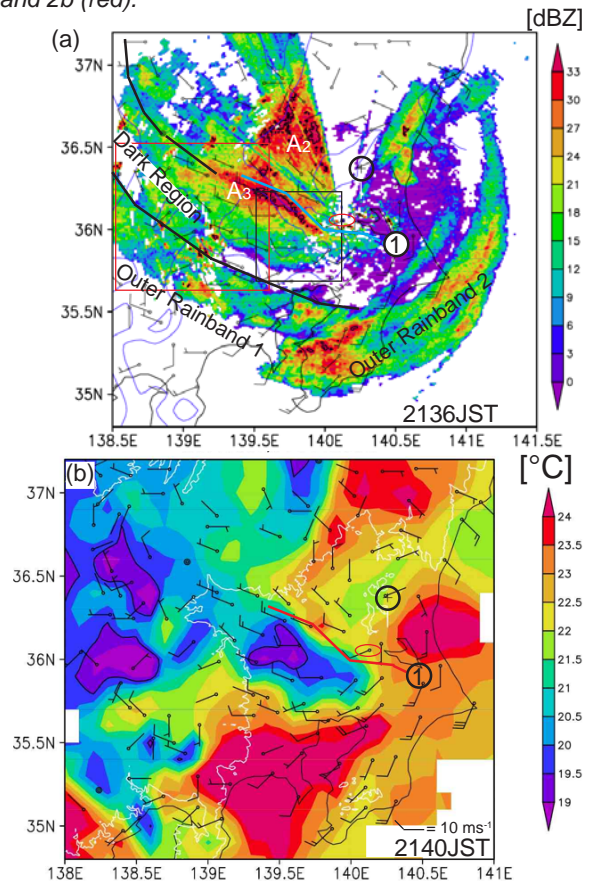


Figure 2. Surface wind barsbs superimposed on reflectivity (a) and surface temperature at sea level (b) on 1 October 2002. The typhoon center is marked by the cross symbol within an open circle. Red ovals denote the location of the MRI. Thin white contours in (b) are the topographic contours of 200 m. Thin blue contours in (a) represent temperature at sea level as in (b) but only at  $20^\circ\text{C}$  and  $22^\circ\text{C}$ .  $A_2$  and  $A_3$  in (a) denote heavy rain regions, and the thick line with a circled 1 in (a) and (b) indicates the location of the thin-line echo in (a). Thick black lines in (a) denote the edges of the dark region in satellite images scanned at 2144 JST. Squares in (a) denote the areas in Figs. 5 (red) and 6 (black), respectively.

### 3.3 Three-Dimensional Analysis of Radial Velocity and Reflectivity Fields

Figures 3a-g show the three-dimensional evolution of radial velocity and reflectivity fields looking south-southwest in the area depicted by a square in Fig. 2a. Figure 3a shows three-dimensional contours of high reflectivity (35 dBZ) and high radial wind speeds (20 m s<sup>-1</sup>) at 2025 JST. The three high-reflectivity regions (regions A<sub>1</sub>, A<sub>2</sub>, and B) are evident. Region A<sub>1</sub> merged with B (Fig. 3b) to form a new high reflectivity region A<sub>3</sub> (Fig. 3c). The height of region A<sub>3</sub> decreased with time (Figs. 2d and 2e) as the thin-line echo formed (Fig. 2f).

High winds started to develop at 2043 JST (Fig. 3c) near the surface after a region of high radial wind entered the region of analysis from the south at altitudes above 7 km (Figs. 3a-d). The size of the area of strong low-level winds increased with time as its edge moved northeast (Figs. 3d-e). After the edge intercepted region A<sub>3</sub> at 2055 JST, A<sub>3</sub> stretched horizontally along the leading edge of the strong low-level winds and formed the thin-line echo (Fig. 3f). Note that the region of the strong low-level winds (Fig. 3e) extends beyond the area where A<sub>1</sub> and B located (Figs. 3a and 3b). This means that the A<sub>3</sub> cannot be a parent thunderstorm for the strong low-level winds.

The strong low-level winds terminated with the arrival of outer rainband 1 (Figs. 3g). Note that some filaments of strong winds extended from the high-wind region aloft to the lower level. These filaments, highlighted by open ovals, occurred just before the onset (Fig. 3b) and in the development stage (2049-2101 JST) of the strong low-level winds (Fig. 3e). These filaments were also observed at 2113 JST (not shown). On the contrary, these filaments were not observed before the onset of the strong low-level winds (Fig. 3a). Unfortunately, detailed features of the filaments in the region of analysis cannot be resolved because of the limited observational resolution of the Doppler radar. However, the observational resolution of the radar is quite high near the MRI site.

Figures 4a-d show the isosurface of strong winds with a radial velocity of 22 m s<sup>-1</sup> in the region depicted by the square in Fig. 2a, at the edge of which the Doppler radar was located. 3-D contours of reflectivities are also plotted in the figures. The figures clearly show that the region of strong low-level winds propagated northeastward.

The base of the high-wind region aloft descended with time (Figs. 4a and 4b) and developed into two funnels, F<sub>1</sub> and F<sub>2</sub> (Fig. 4b), ahead of the region of strong low-level winds. The funnel F<sub>2</sub> descended at a speed of 4.3 m s<sup>-1</sup>, reaching the ground by 2125 JST (Fig. 4c).

F<sub>2</sub> was likely reduced its translation speed after reaching the ground at 2137 JST (Fig. 4d). On the other hand, the relatively high reflectivity region (27 dBZ in Fig. 4d) corresponded to the thin-line echo was located ahead of F<sub>2</sub>, suggesting the region of strong low-level winds overtook the funnels by 2137 JST. The mean body depth of the region of strong low-level winds increased from 1.2 km at 2119 JST (Fig. 4b) to 2 km by the time, suggesting vertical momentum transport occurred. To investigate the vertical conservation of momentum in the funnel F<sub>2</sub>, we define horizontal momentum per unit volume  $P$  as,

$$P = \rho (-Vr + w \sin\theta) / \cos\theta, \quad (1)$$

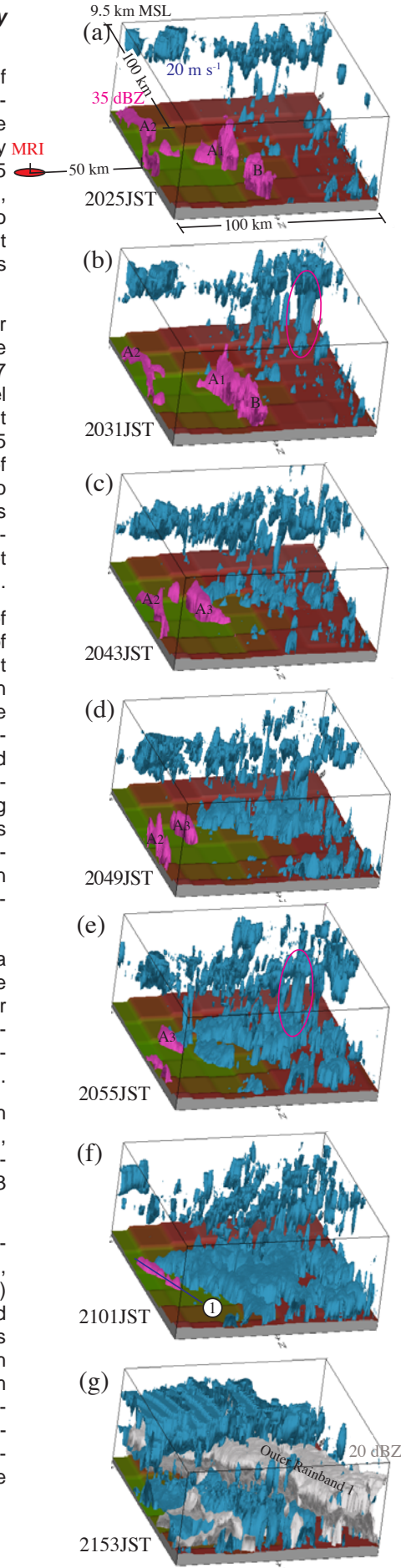


Figure 3. Three-dimensional contours of reflectivity and high wind looking south-southwest on 1 October 2002, in the region depicted in Fig. 2a. The observation time is shown in the lower-left of each image. Dark pink surfaces in (a)–(f) denote reflectivity at 35 dBZ, while blue surfaces in each image represent radial velocities at 20 m s<sup>-1</sup>. Light gray surfaces in (g) represent reflectivity at 20 dBZ, which corresponds to the outer rainband 1 in Fig. 2a. Open ovals in (b) and (e) denote areas of high-wind filaments. The blue line with a circled 1 in (f) denotes the first thin-line echo. A closed oval in (a) denotes the location of the MRI.

where  $\rho$  is atmospheric density at given altitude measured with the radiosonde,  $V_r$  is radial velocity measured with the Doppler radar,  $w$  is the vertical component in  $F_2$ , and  $\theta$  is the elevation angle of the Doppler radar. The mean and the standard deviation of  $P$  for altitudes from 500 m AGL and 4000 m AGL were  $24.1 \text{ kg m}^{-2} \text{ s}^{-1}$  and  $0.4 \text{ kg m}^{-2} \text{ s}^{-1}$ , respectively. In the derivation, vertical velocity  $w$  is assumed to be  $-4.3 \text{ m s}^{-1}$  at all heights. The STD was surprisingly small ( $\sim 1.8\%$ ) with respect to the mean, meaning momentum was vertically conserved.

On the other hand, the presence of a nose and/or a head, which is often observed with a gust front, is not obvious in the figures. This could be because the spatial and temporal resolutions of the Doppler radar observations were too coarse to capture these detailed features of the cold airflow. Fortunately, wind profiler and tower observations captured these features.

### 3.4 Horizontal and Vertical Wind Vector Profiles

Figure 5 shows time–height cross sections of the horizontal and vertical component of wind derived from the wind profiler and the tower. Time runs from right to left. Red contours are isotachs of wind speed in the propagation direction of the thin-line echo averaged over 2 min. Gaps in the contours occur where low quality profiler data were rejected.

The contours of horizontal wind speed depict an elevated nose and head-like structures near the surface. The high wind region aloft at 2140 JST could be a part of the funnel  $F_2$  (Fig. 4d). The profiler captured the strong upward air motion ( $\sim 2 \text{ m s}^{-1}$ ) at the passage of the thin-line echo at 2150 JST. In addition, Fig. 5 also shows that the strong winds just behind the first thin-line echo exceeded the propagation speed of the first thin-line echo ( $19.5 \text{ m s}^{-1}$ ) at altitudes below 1000 m, except close to the surface. This means that a feeder flow, which is a prominent and ubiquitous feature to a gravity current [3], existed.

## 4 CONCLUSION

Since the cold airflow associated with the thin-line echo had features unique to a gravity current, we conclude that the first thin-line echo was due to a gust front. However, this gust front cannot be categorized as a so-called thunderstorm gust front, because it had no parent convective storm behind: rather, Doppler radar and wind profiler observations suggest that relatively strong downdrafts ( $\sim 4 \text{ m s}^{-1}$ ) in the weak precipitation region and large momentum transported by the downdrafts from aloft ( $\sim 4 \text{ km}$ ) to lower levels produced and maintained near-surface high winds behind the gust front. For the details of this study, see [4].

## REFERENCES

- [1] Powell, M. D., 1990: Boundary layer structure and dynamics in outer hurricane rainbands. *Mon. Wea. Rev.*, **118**, pp. 891-917.
- [2] Corfidi, S. F., 2003: Cold pools and MCS propagation. *Wea. Forecasting.*, **18**, pp. 997-1017.
- [3] Smith, R. K. and M. J. Reeder, 1988: On the movement and low-level structure of cold fronts. *Mon. Wea. Rev.*, **116**, pp. 1927-1944.
- [4] Adachi, A. and T. Kobayashi, 2009: A nonclassical gust front and a solitary wave embedded within a typhoon. *JMSJ*, **87**, pp. 57-82.

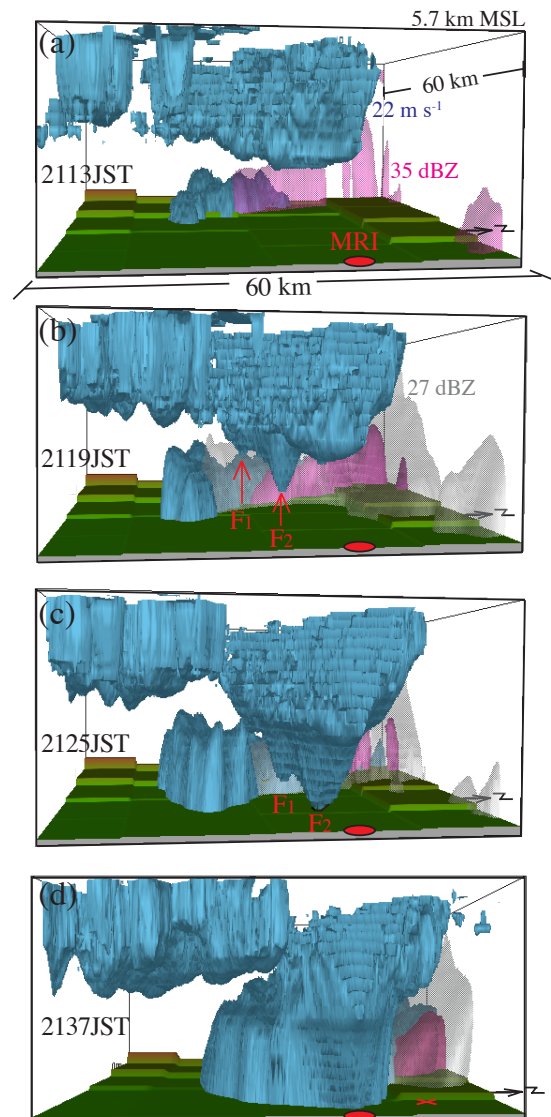


Figure 4. Three-dimensional contours of reflectivity and high wind looking west-northwest on 1 October 2002, in the region depicted in Fig. 2a. Arrows in (b) indicate the locations of two high-wind funnels,  $F_1$  and  $F_2$ . A black line at the bottom of  $F_2$  in (c) outlines a portion of the touchdown area.

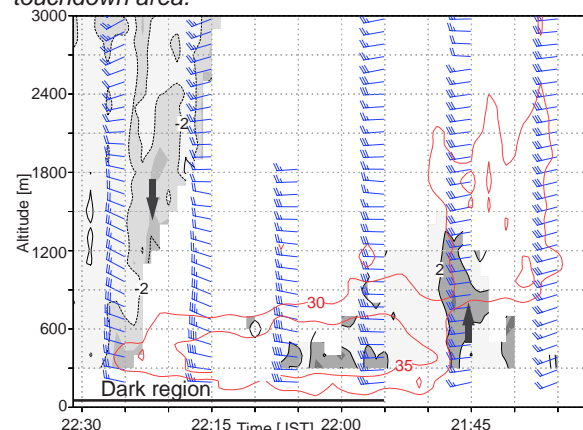


Figure 5. Time–height cross section of horizontal wind vectors and vertical motion derived from the wind profiler on 1 October 2002. Time progresses from right to left. Arrows denote the direction of the vertical airflow. The wind speed in the front propagation direction measured with the profiler and the tower is also plotted with red contours to represent the low-level high winds.